



HAL
open science

Swirling of vesicles: Shapes and dynamics in Poiseuille flow as a model of RBC microcirculation

Jinming Lyu, Paul G. Chen, Alexander Farutin, Marc Jaeger, Chaouqi Misbah, Marc Leonetti

► **To cite this version:**

Jinming Lyu, Paul G. Chen, Alexander Farutin, Marc Jaeger, Chaouqi Misbah, et al.. Swirling of vesicles: Shapes and dynamics in Poiseuille flow as a model of RBC microcirculation. *Physical Review Fluids*, 2023, 8 (2), pp.L021602. 10.1103/PhysRevFluids.8.L021602 . hal-03979358v2

HAL Id: hal-03979358

<https://hal.science/hal-03979358v2>

Submitted on 10 Feb 2023

HAL is a multi-disciplinary open access archive for the deposit and dissemination of scientific research documents, whether they are published or not. The documents may come from teaching and research institutions in France or abroad, or from public or private research centers.

L'archive ouverte pluridisciplinaire **HAL**, est destinée au dépôt et à la diffusion de documents scientifiques de niveau recherche, publiés ou non, émanant des établissements d'enseignement et de recherche français ou étrangers, des laboratoires publics ou privés.

Swirling of vesicles: Shapes and dynamics in Poiseuille flow as a model of RBC microcirculation

Jinming Lyu,¹ Paul G. Chen,¹ Alexander Farutin,² Marc Jaeger,¹ Chaouqi Misbah,² and Marc Leonetti^{3, *}

¹*Aix Marseille Univ, CNRS, Centrale Marseille, M2P2, Marseille, France*

²*Univ. Grenoble Alpes, CNRS, LIPhy, Grenoble, France*

³*Aix Marseille Univ, CNRS, CINaM, Marseille, France*

(Dated: February 1, 2023)

We report on a systematic numerical exploration of the vesicle dynamics in a channel, which is a model of red blood cells in microcirculation. We find a spontaneous transition, called swirling, from straight motion with axisymmetric shape to a motion along a helix with a stationary deformed shape that rolls on itself and spins around the flow direction. We also report on a planar oscillatory motion of the mass center, called three-dimensional snaking for which the shape deforms periodically. Both emerge from supercritical pitchfork bifurcation with the same threshold. The universality of these oscillatory dynamics emerges from Hopf bifurcations with two order parameters. These two oscillatory dynamics are put in the context of vesicle shape and dynamics in the parameter space of reduced volume v , capillary number, and confinement. Phase diagrams are established for $v = 0.95$, $v = 0.9$, and $v = 0.85$ showing that oscillatory dynamics appears if the vesicle is sufficiently deflated. Stationary shapes (parachute/bullet/peanut, croissant, and slipper) are fixed points, while swirling and snaking are characterized by two limit cycles.

I. INTRODUCTION

Soft particles such as vesicles, red blood cells (RBCs), compound droplets, capsules, and elastic fibers display rich dynamic behaviors in linear and quadratic flows [1–12]. If the zoology of dynamics shares some common characteristics, the so-called tank treading, for example, it may also differ by bifurcation dynamics of each soft particle. A vesicle in shear flow does not exhibit swinging contrary to capsule and red blood cell, for example, demonstrating the complexity to understand deeply the coupling between shape and motion.

If deciphering the complex dynamics of such deformable particles is still an open issue, the challenge is also to measure some physical and mechanical membrane properties by an inverse method comparing experimental shapes to numerical ones [13–17]. In the high-throughput shape recognition of RBCs moving in a microcapillary for which a few images per RBC are captured, it is essential to select relevant physical parameters (e.g., flow rate and confinement) to avoid any oscillatory, chaotic or transient dynamics for efficient shape recognition [18, 19].

Recently, a planar oscillatory dynamics in Poiseuille flow, called snaking, was predicted numerically in 2D for vesicle with a deflation equal to RBC [20] and in 3D for RBC model with shear elasticity [21, 22]. The center of mass oscillates in a plane while the particle moves along a microcapillary and the shape deforms. Living systems such as listeria bacteria, keratinocytes, and paramecium also exhibit oscillatory dynamics, but the center of mass moves along a helix [23–25]. Is this possible with a passive soft particle such as a vesicle suggesting that these motions are universal and shared by any entity, be it driven out of equilibrium, or active?

Here, we focus on a three-dimensional (3D) vesicle moving in a microcapillary, i.e., a bounded Poiseuille flow. This configuration is a model of RBC in microcirculation in the dilute regime. While the dynamics in a shear flow are well understood, this is much less the case in a Poiseuille flow with the following questions for example: Does the snaking motion exist in 3D, or is this specific to 2D? Can we expect novel oscillatory dynamics such as those observed experimentally in living systems? How do the new oscillating dynamics relate to the stationary solutions in the parameter space?

II. PROBLEM FORMULATION

A. Governing equations

We consider a vesicle of volume $V = (4/3)\pi R_0^3$ and area A in a capillary of radius R_c . In a typical experiment with vesicles, the length scale is $10\ \mu\text{m}$, the velocity $1\text{--}100\ \mu\text{m s}^{-1}$, and viscosity in the range $1\text{--}10\ \text{mPa s}$. Considering

* marc.leonetti@univ-amu.fr

the density of water, the Reynolds number is of the order of 10^{-4} , leading to negligible inertia contribution in the momentum equation. As the fluids are incompressible, velocity \mathbf{v} and pressure p satisfy the Stokes equations inside and outside the vesicle:

$$-\nabla p + \eta \Delta \mathbf{v} = \nabla \cdot \boldsymbol{\sigma} = \mathbf{0}, \quad \nabla \cdot \mathbf{v} = 0, \quad (1)$$

where η is the viscosity and $\boldsymbol{\sigma}$ the Newtonian stress tensor.

Far from the vesicle, the unperturbed flow \mathbf{V}_∞ is imposed:

$$\mathbf{V}_\infty(\mathbf{x}) = V_m (1 - r^2/R_c^2) \mathbf{e}_x, \quad r \leq R_c, \quad (2)$$

where $r^2 = y^2 + z^2$, $\mathbf{x} = (x, y, z)$ and V_m is the velocity at the centerline.

The material interface of vesicles is a lipid bilayer of approximately 4 nm thickness. Lipids are free to move along each monolayer. The exchange of lipids between monolayers and their friction [26] is neglected. The area compressibility coefficient is very large meaning that in the range of experimental shear stress, the area is locally conserved, which results in

$$\nabla_s \cdot \mathbf{v} = 0, \quad (3)$$

where $\nabla_s = (\mathbf{I} - \mathbf{n}\mathbf{n}) \cdot \nabla$ is the surface gradient operator.

Finally, the membrane is a two-dimensional (2D) incompressible fluid with bending resistance, leading to out-of-plane membrane force. Its free energy is the so-called Helfrich energy, with an additional term ensuring the two-dimensional incompressibility:

$$F_m = \frac{\kappa}{2} \int_S [2H(\mathbf{x})]^2 dS + \int_S \gamma(\mathbf{x}) dS, \quad (4)$$

where $H(\mathbf{x})$ is the local mean curvature and $\gamma(\mathbf{x})$ a local Lagrange multiplier with the dimension of a surface tension.

The conditions of coupling between the interface and bulk flows result from the conditions of continuity and mechanical equilibrium at the interface:

$$\mathbf{v}_o = \mathbf{v}_i, \quad (5)$$

$$[\boldsymbol{\sigma}_o - \boldsymbol{\sigma}_i] \mathbf{n} + \mathbf{f}_m = \mathbf{0}, \quad (6)$$

where \mathbf{f}_m is the membrane force density derived from Eq. (4) and \mathbf{n} the normal unit vector. The membrane shear dissipation [27, 28] is neglected, unlike the case of polymersomes, for which it is predominant [29, 30].

B. Dimensionless numbers and physical quantities

The reference length R_0 is defined by the volume V :

$$L_{\text{ref}} = R_0, \quad V = \frac{4}{3} \pi R_0^3, \quad (7)$$

the reference time by the viscous relaxation of a bending mode:

$$T_{\text{ref}} = \frac{\eta R_0^3}{\kappa}, \quad (8)$$

and the pressure and the hydrodynamic stress tensor by

$$p_{\text{ref}} = \frac{\kappa}{R_0^3}. \quad (9)$$

Vesicles are deflated, i.e., their area A is larger than the area of a sphere of the same volume V . This deflation allows the system to vary its shape driving by the mechanical equilibrium at the interface. This property is quantified by the reduced volume v or the excess area. We choose the reduced volume:

$$v = \frac{V}{\frac{4}{3} \pi (\frac{A}{4\pi})^{3/2}} = (4\pi)^{3/2} \frac{R_0^3}{A^{3/2}}. \quad (10)$$

The ability to deform more or less freely from the wall is evaluated by the confinement number C_n :

$$C_n = \frac{R_0}{R_c}. \quad (11)$$

When C_n becomes small, the dynamic behavior in unbounded Poiseuille flow is recovered.

The capillary number Ca measures the competition between the hydrodynamic stress of the order of $\eta(\partial V_\infty/\partial r)_{r=R_0/2}$ and the bending response of the membrane κ/R_0^2 :

$$Ca = \frac{\eta V_m R_0^2}{\kappa} \left(\frac{R_0}{R_c} \right)^2. \quad (12)$$

This expression can also be rewritten with the flow curvature V_m/R_c^2 , making the connection between unbounded and bounded limits more simple.

C. Numerical formulation

The Stokes equations in multiphase systems can be converted into a boundary integral formulation; see Ref. [31] for generalities and Refs. [32–34] for vesicles. As underlined in Refs. [35–37], 3D computations of vesicles in *bounded* configuration are still a challenge. In this paper we use an isogeometric FEM-BEM method based on loop subdivision surfaces used both for the finite element solver for membrane forces (FEM) and for the boundary element method (BEM) for the fluid solver [38]. The confined geometry needs an additional specific method to take into account the no-slip condition at the wall; see Ref. [39] for details on the length of the capillary, its meshing, and the validation. Here, all the simulations are performed with 1280 elements for the vesicle membrane and without viscosity contrast. There is a remeshing algorithm with criteria based on local curvature, area element, and angles of an element, which allows preservation of a regular mesh, even in some cases with high curvature [40].

Computations are performed by decreasing the reduced volume by step $\Delta v = 0.05$ until a new dynamics is achieved. The range of reduced volume spans from $v = 0.95$ to $v = 0.85$, the capillary number from $Ca = 0.1$ to $Ca = 10$, the confinement from $C_n^{-1} = 1$ to $C_n^{-1} = 8$. We also investigate the unbounded limit with Ref. [38] to compare with $C_n^{-1} = 8$. As explained further, the cases $v = 0.75$ and $v = 0.8$ have been performed for one set of parameters to check the universality of oscillatory dynamics.

We vary the initial shape of the vesicle, the lateral position of its center of mass $y_{CM}(0) \equiv H$, and the tilt angle with respect to the flow axis $\theta_y(0)$ of its longest axis in the (x, z) plane in order to explore stability of solutions. We have verified that the kind of dynamics does not depend on the choice of the initial perturbation, y axis, z axis, or a mixing. For the sake of simplicity, the results are presented as if the perturbation was always along the y axis. Generally, the initial shape is the one at thermal equilibrium. We checked that an initial prolate shape leads to the same results in several cases. The value of H has been varied from $0.0005 \ll 1$ to $\max(H) \approx C_n^{-1} - 0.4$. Smaller values of H are preferred for studying the linear stability far from the threshold and the nature of bifurcation. Details will be provided in the last paragraph of Sec. IV. Larger values of H are used to establish the phase diagram and the role of initial conditions close to the swirling-to-slipper transition. In most cases, $\theta_y(0)$ was equal to 0° or $\pm 10^\circ$. For one set parameters ($Ca = 1$, C_n^{-1}), we have verified that swirling always appears whatever the initial angle between 5° and 45° . When the stability of a solution branch is investigated, such as the axisymmetric one or the snaking one for example, the initial shape is that of the branch; its orientation and radial position are generally varied with 10° and moved by 0.0005. If necessary, we will specify the conditions in the text.

III. SHAPES OF SLIGHTLY DEFLATED VESICLES IN POISEUILLE FLOW

First, we have systematically explored the quasispherical case ($v \geq 0.9$). Whatever the initial perturbation [H , $\theta_y(0)$], Ca , and C_n , all the final states—axisymmetric shape, croissant, and slipper—are stationary. Bullet and parachute shapes are axisymmetric with a positive and negative curvature at the rear, respectively [36, 41]. Furthermore, there is no membrane flow. Croissantlike shapes are symmetric to (y, z) and (x, z) planes, already observed in unbounded [42] and bounded cases [35, 36]. There are four vortices at the membrane. Slippers are stationary out-of-axis shapes, already observed in 2D [43], in the 3D unbounded case [42], and recently in the 3D bounded case [35, 36].

The phase diagrams have been established for $v = 0.95$ and $v = 0.9$. As shown in Fig. 1, they are qualitatively similar. The transition slipper \rightarrow croissant \rightarrow parachute is shifted to higher capillary number when the reduced

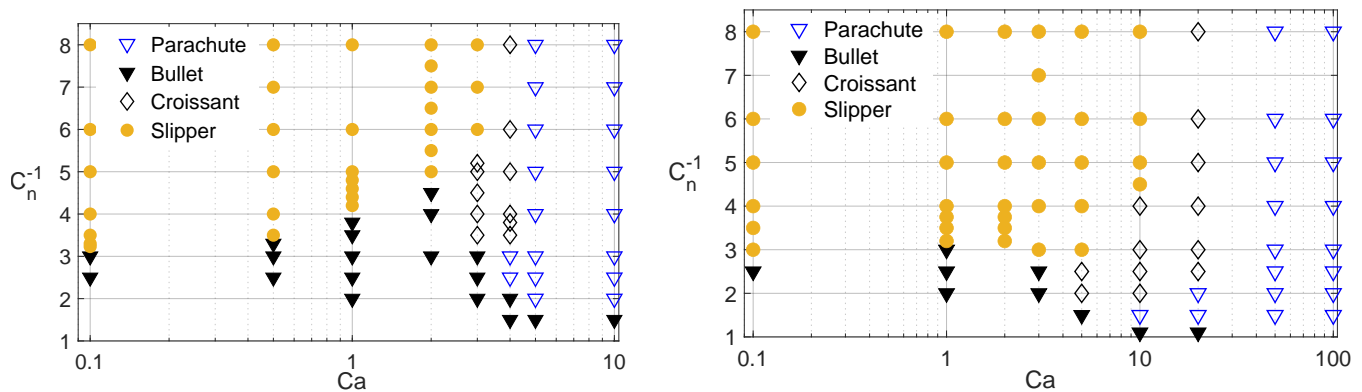


FIG. 1. Phase diagram of a confined vesicle with $v = 0.95$ (left) and $v = 0.9$ (right) in a Poiseuille flow in the parameter space (Ca, C_n) . Only stationary shapes exist.

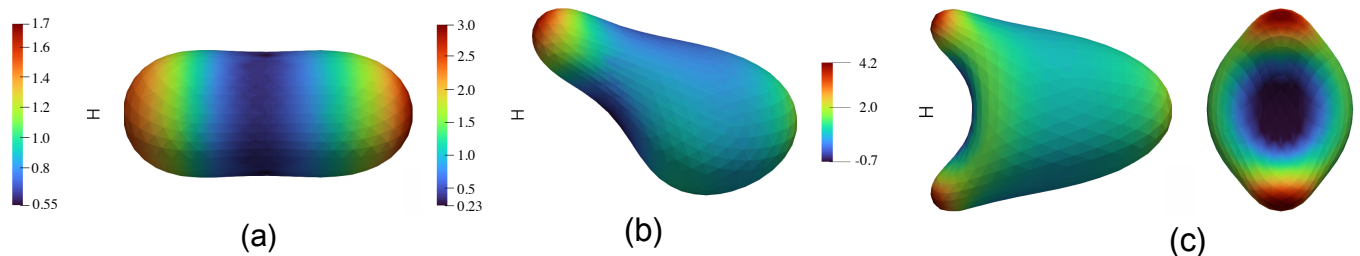


FIG. 2. Examples of stationary shapes with $v = 0.85$. (a) Peanut shape (axisymmetric): $Ca = 1$ and $C_n^{-1} = 1.8$. (b) Slipper shape: $Ca = 3$ and $C_n^{-1} = 5$. (c) Croissant shape: $Ca = 20$ and $C_n^{-1} = 2$. See text for details on the properties of each shape and on parachute. The color code corresponds to the mean curvature H .

volume is decreased. We observe a croissantlike shape for $C_n^{-1} = 8$, a solution also obtained in the unbounded limit. While only slippers are solutions with $C_n^{-1} = 5$ and $v = 0.9$ whatever the capillary number in Ref. [36], we still observe the transition slipper \rightarrow croissant \rightarrow parachute in this regime. We didn't observe periodic oscillations in the unconfined limit with $v = 0.9$ and $Ca = 4$ as reported in Ref. [36].

IV. SHAPES AND DYNAMICS OF DEFLATED VESICLES IN POISEUILLE FLOW

Next we consider smaller v , $v = 0.85$. In weak confinement, namely, the unbounded limit, we observe similar shapes as slightly deflated vesicles: axisymmetric (parachute), slipper [Fig. 2(b)], and croissant [Fig. 2(c)]. In strong confinement $C_n \geq 0.8$, whatever the initial position H and the capillary number, the final state is stationary and axisymmetric, as observed in experiments [41, 45]. For small and moderate capillary numbers, the axisymmetric shape is called peanut, see Fig. 2(a).

As the channel diameter is increased, this state becomes unstable in favor of a nonstationary mode. Unexpectedly, this mode cannot be identified as snaking but is instead what we call swirling [Fig. 3(b)]. Swirling is peculiar, as the shape of the vesicle is fixed but its lateral position and orientation change periodically (Fig. 4). The vesicle moves along a helix while rotating about the flow direction (Fig. 4). The direction of the longest semiaxis L_1 varies periodically. Considering its projections in the planes (x, y) , (x, z) , and (y, z) , three angles θ_{xy} , θ_{xz} , and θ_{yz} are defined, respectively. While the trajectory is characterized by a fixed distance R_{CM} of the vesicle from the channel axis, the positions (Y_{CM}, Z_{CM}) of the mass center oscillate in quadrature.

In order to gain further insight into the origin of the swirling and its relation to snaking, we have set $\theta_y(0) = 0$, thus imposing the $z \rightarrow -z$ symmetry. The oscillatory dynamics of the vesicle center of mass is confined to the (x, y) plane [Fig. 3(a)] and is synchronized with deformation of the vesicle [Figs. 5(a) and 5(c)]. This mode is characterized

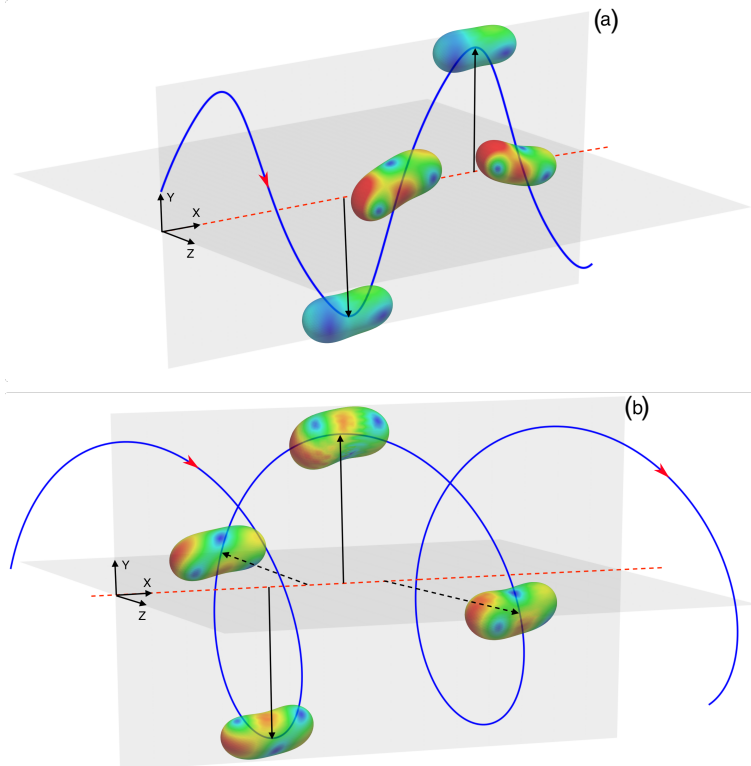


FIG. 3. 3D snaking and swirling: $v = 0.85$, $Ca = 1$, and $C_n^{-1} = 2.75$. (a) Snaking: $\theta_y(0) = 0$. The center of mass oscillates in the plane (x, y) : blue curve. The shape deforms. (b) Swirling: $\theta_y(0) \neq 0$. The center of mass moves along a helix (blue curve) centered on the microcapillary's axis, the x axis. The shape does not deform and turns around the helix. The black arrows point outward to the center of mass with solid and dashed lines in the planes (x, y) and (x, z) , respectively. Color code corresponds to interfacial velocity; see movies in Ref. [44].

by a limit cycle as shown in Fig. 5(b). The dependence on H will be discussed further. We thus recover the 3D analog of the snaking motion reported in 2D [20]. Breaking the $z \rightarrow -z$ symmetry results in the instability of the snaking, and a small perturbation of θ_y leads to swirling, see Fig. 5(d).

As shown in Figs. 5(a) and 5(b), where all the parameters are the same except H , slipper and snaking are unexpectedly two solutions varying H from 0.0005 to $H = 0.3$. Each basin of attraction of solutions depends on H , at least in a part of parameter space. To gain insight, we established the phase diagram of shapes and dynamics in (C_n, H) space in the case $Ca = 1$, see Fig. 5(e). The possible position of the initial thermodynamic shape is restricted to a range $[0, H_{max}]$ as mentioned in Sec. II C. H_{max} corresponds to the dotted line. If the confinement is large, only axisymmetric shapes exist and the axi \rightarrow snaking transition does not depend on H (dashed line). Far from the center line, i.e., H between 0.06 and H_{max} , the snaking \rightarrow slipper does not depend on H contrary to close to the center line ($H < 0.06$) where there is a weak dependence. Note that thanks to Fig. 5(d), we know that the snaking domain also corresponds to swirling.

The bifurcation diagram of the observed motions is shown in Fig. 6(a). The solutions are obtained by slightly off-centering the vesicle in the y direction. We use two initial orientations: the $z \rightarrow -z$ symmetric orientation [$\theta_y(0) = 0$] to track the snaking branch and a tilt towards the z axis ($\theta_y(0) > 0$) to track the swirling branch. Below a critical value $C_n^{-1} = C_{nc}^{-1} = 1.98 \pm 0.015$, the mass center comes back to the centerline defining the stable branch of axisymmetric shapes (green triangles). Above the critical value, the centered solution is unstable as checked by small perturbation of the lateral position. Two branches of solutions emerge at this point: the swirling branch (black circles), which is unconditionally stable, and the snaking branch (oscillation amplitude is shown as blue squares), which is stable only with respect to perturbations that respect the $z \rightarrow -z$ symmetry. Indeed, the three black arrows with $C_n^{-1} = 2.3, 2.75$, and 2.9 correspond to the perturbation where the axisymmetric shape is turned by $\theta_y(0) = 10^\circ$. The result is the same if the initial shape is at thermodynamic equilibrium. If there is also a perturbation of the radial position, the time to join the swirling branch is decreased (other points). The black arrow with $C_n^{-1} = 3.1$ corresponds to the perturbation where the axisymmetric shape is turned by $\theta_y(0) = 10^\circ$, but in this case the swirling branch does not exist anymore. The final state is a slipper (orange circles). The blue arrows with $C_n^{-1} = 2.3$ and 2.75 correspond

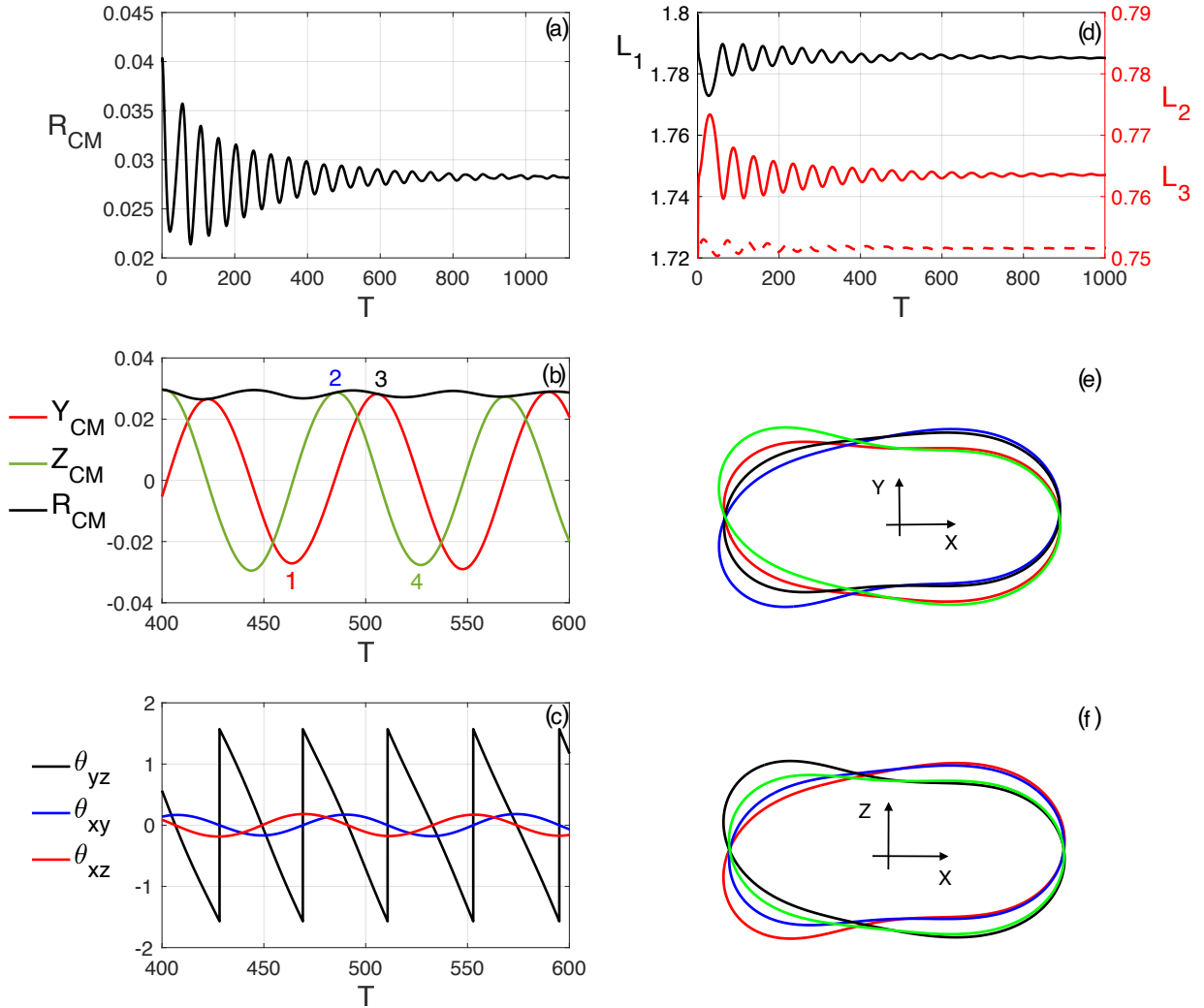


FIG. 4. Swirling: $v = 0.85$, $Ca = 1$, $C_n^{-1} = 2.75$, and $\theta_y(0) = 10^\circ$. (a) Temporal variation of the radial position of the mass center R_{CM} . (b) Temporal variation of the cartesian positions (Y_{CM} , Z_{CM}). (c) The angles θ_{xy} and θ_{xz} of the longest semiaxis L_1 oscillate in quadrature in the planes (x, y) and (x, z) , respectively. The angle θ_{yz} of L_1 in the plane (y, z) varies linearly with time. The inset refers to the shape and its rotation (yellow arrow) during one period seen from the rear at four times 1–4 (color code). (d) The lengths L_j of three semiaxis of the equivalent ellipsoid tend to a constant. (e) Cross sections of the shapes in the plane (x, y) at the times 1–4 defined in (b). (f) Cross-sections of the shapes in the plane (x, z) . The color code corresponds to numbers 1–4 defined in (b).

to the perturbation of snaking with a rotation of $\theta_y(0) = 10^\circ$. The system evolves to swirling. With $C_n^{-1} = 3$, the system evolves to slipper. Finally, to be complete, the three first points with $1.98 < C_n^{-1} < 2$ were obtained beginning with the solution with $C_n^{-1} = 2.05$ to decrease the time of calculations. Indeed, close to the threshold, there is a critical slowdown. Both for snaking and swirling the amplitudes grow continuously from 0 and scale as $|C_n - C_{nc}|^{1/2}$ close to the critical point, a signature of supercritical pitchfork bifurcation considering the accuracy of simulations [46]. Swirling is stable whatever the perturbation is in the range of confinement shown in Fig. 6(a). If $C_n^{-1} \geq 3 \pm 0.05$, swirling, snaking, and axisymmetric shape are unstable. The system reaches the slipper branch of solution (orange circle). For lower C_n^{-1} , this branch is only obtained if the initial position is larger than a critical value. Finally, the phase diagram in the space (Ca, C_n) is shown in Fig. 6(b).

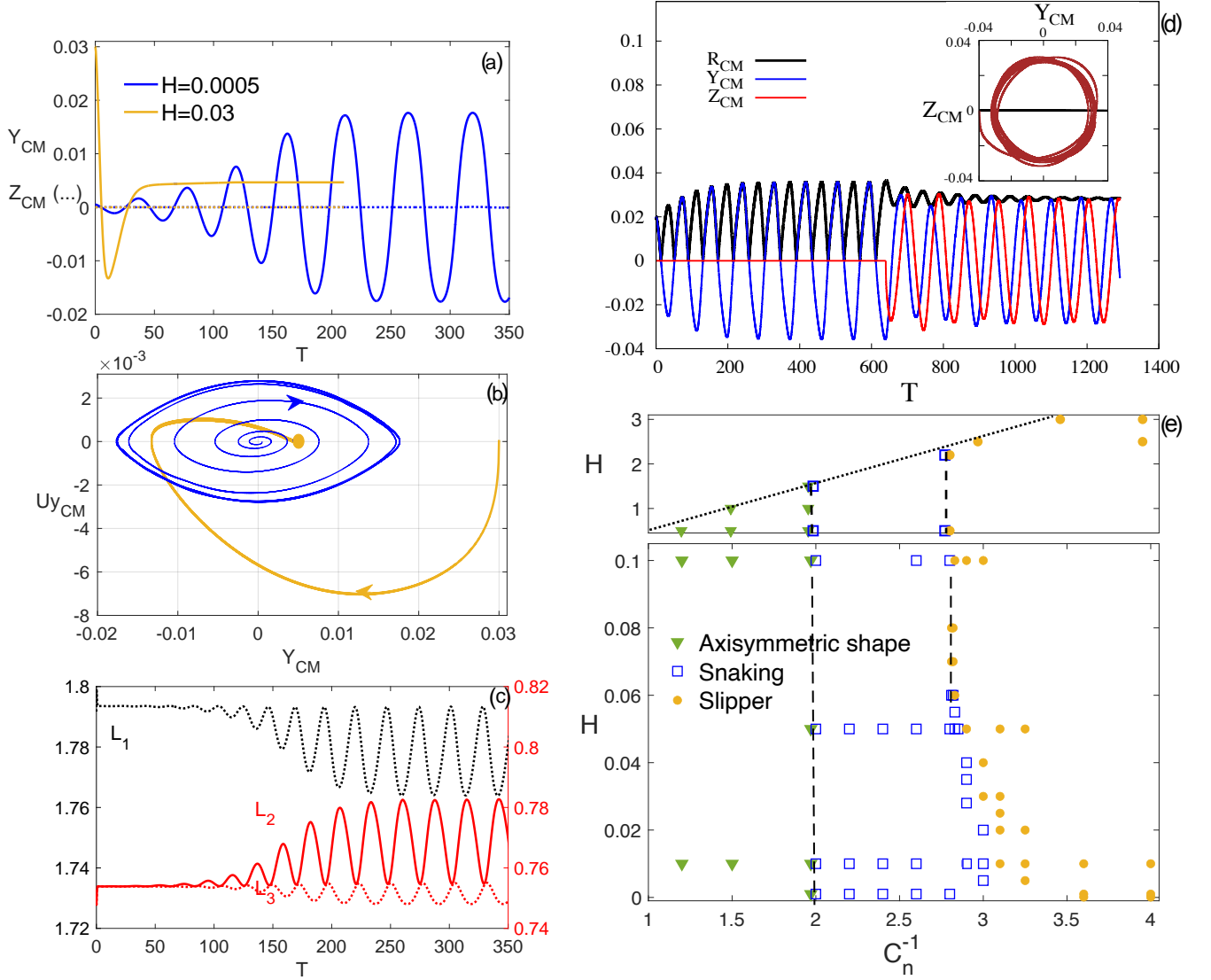


FIG. 5. (Left panel) 3D snaking: $v = 0.85$, $Ca = 2.3$, $C_n^{-1} = 2.5$, and $\theta_y(0) = 0^\circ$. (a) The same initial shape evolves to slipper (orange, $H = 0.03$) or snaking (blue, $H = 0.0005$) following the initial position H ; see the blue and orange arrows for the path. Snaking is an oscillation of the mass center position in a plane, here (x, y) . (b) Phase portrait of (a) showing the fixed point (slipper) and limit cycle (snaking). (c) The 3D shape oscillates during snaking, temporal variations of the lengths L_j of the three semi-axis of the equivalent ellipsoid. (Right panel) (d) Transition from 3D snaking to swirling after a rotation $\theta_y = 10^\circ$ of the long axis angle around y axis: $v = 0.85$, $Ca = 1$, and $C_n^{-1} = 2.75$. Insert: In the phase space (Y_{CM}, Z_{CM}) , the black line corresponds to 3D snaking and the red circle to the limit cycle of swirling. (e) Phase diagram in the parameter space (C_n^{-1}, H) with $Ca = 1$. For steric reasons, the domain above the dotted line is not relevant.

V. DISCUSSION AND CONCLUSION

We provided the first observation and nonlinear characterization of snaking and swirling for vesicles in 3D. Snaking has been observed in 2D with $v = 0.6$, as well as for 3D models of RBCs. Here we have shown that swirling is in fact the most unstable oscillatory mode for a vesicle moving along a microcapillary in the range of investigated parameters, thereby highlighting the role of the space dimension in such dynamics.

Snaking has been observed in 2D with $v = 0.6$, which supports its application to RBCs. We also observed swirling in 3D with $Ca = 1$, $C_n = 0.4$, $v = 0.8$, 0.75 , and $v = 0.7$, ensuring its general relevance. Considering parameters such as $R_0 = 3 \mu\text{m}$, $\eta = 10^{-3} \text{ Pa s}$, $\kappa = 10^{-19} \text{ J}$ [47], $C_n = 0.4$ leads to a maximum velocity of $100 \mu\text{m s}^{-1}$. The range of relevant velocities in microfluidic chips is $1\text{--}100 \mu\text{m s}^{-1}$. The period is of the order of 20 s. The length covered during a period varies between $20 \mu\text{m}$ and 2 mm. The lowest dynamics is measurable with classic microfluidics, while the

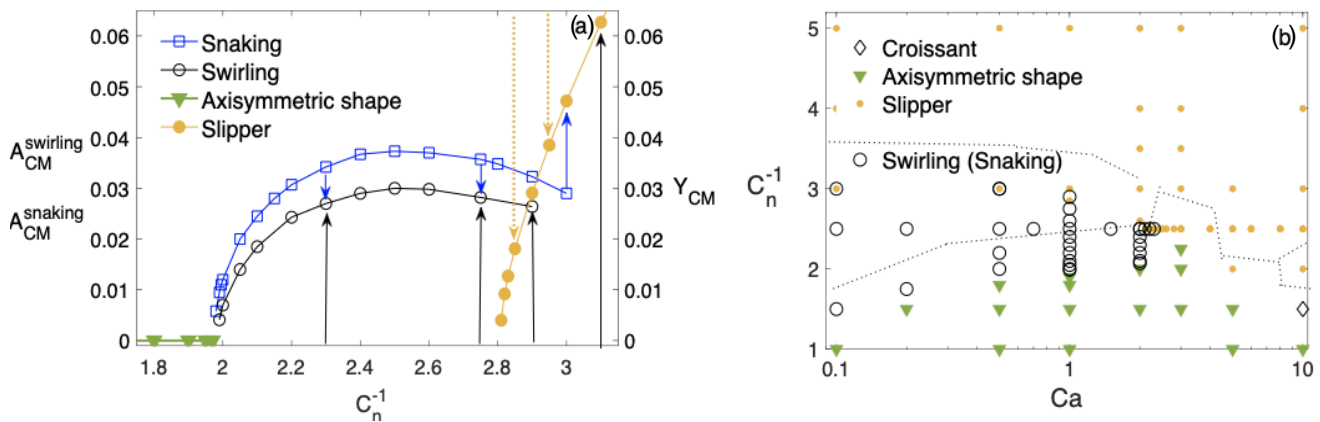


FIG. 6. Analysis of stability. (a) Diagram of bifurcation: $v = 0.85$ and $Ca = 1$. Order parameters are the position of the mass center (Y_{CM}) if the mode is stationary and the amplitudes (A_{CM}) if oscillating. Above $C_n^{-1} = 2.95 \pm 0.05$, the vesicle transits to the slipper branch whatever the perturbation. This branch is extended to zero by considering initially $H = 0.1$. Below $C_n^{-1} = 2.95 \pm 0.05$, the initial shape is axisymmetric and $H = 0.0005$. The swirling (snaking) branch is reached with $\theta_y(0) = 10^\circ$ (0°). Blue arrows correspond to the snaking-to-swirling transition when a perturbation breaking the mirror symmetry ($\theta_y = 10^\circ$) is applied to snaking. Below $C_n^{-1} = 1.98 \pm 0.015$, only the axisymmetric branch exists whatever the perturbation. (b) Phase diagram in the plane (Ca, C_n^{-1}) .

largest one needs probably a tracking of the shape along the pipe, e.g., a pulled glass on a motorized stage. Swirling can be characterized by the rotation of the protuberance at the rear of the vesicle as shown in Fig. 5(c) and Figs. 4(e) and 4(f), which is of the order of the vesicle's size.

Our study shows that in 3D, snaking and swirling are deeply interconnected. Indeed, Fig. 6(a) shows that preventing the breaking of the $z \rightarrow -z$ symmetry in the vesicle dynamics changes the vesicle dynamics from swirling to snaking. This suggests that the swirling dynamics can be represented to the leading approximation as a superposition of snaking dynamics in two orthogonal planes (x, y) and (x, z) , where the position oscillations along the y and z directions have the same amplitudes but different phases. The phase shift between the oscillation of Y_{CM} and Z_{CM} can be either $\pi/2$ or $-\pi/2$. These two possibilities correspond to either clockwise or counterclockwise swirling which can be selected by the sign of $\theta_y(0) = \pm 10^\circ$. The vesicle thus acquires chirality through spontaneous symmetry breaking. This chirality is also manifested in the vesicle shapes, as the shapes observed for two different swirling directions differ by a mirror symmetry and cannot be made identical by any rotation of the space. In this view the swirling motion is the ultimate state of the symmetry loss sequence parachute \rightarrow croissant \rightarrow slipper \rightarrow swirling, where the last symmetry lost is the mirror plane of the slipper.

Helical trajectories in a pipe or in an unbounded fluid have been observed also for microswimmers [48, 49] and other cells [23–25], highlighting their universality. The oscillatory nature of swirling and snaking clearly suggests a Hopf bifurcation at their origin. Here, however, we are dealing with a nonclassical case of Hopf bifurcation, because we have two order parameters, corresponding to the vesicle displacements in y and z directions (Y_{CM} and Z_{CM}), which are independent in the linear approximation but are coupled at higher order. Our results suggest that a weakly nonlinear analysis based on the symmetries of the configuration should be possible. Finally, the numerical simulations should be extended to include spontaneous curvature, area difference elasticity, viscosity contrast, or shear elasticity for RBCs. Since the two motions have been shown to be universal, we expect that including further ingredients should only affect our results quantitatively.

In summary, dynamics of vesicles in Stokes flow reveals rich nonlinear dynamics with stationary modes, namely, fixed points (bullet, parachute, slipper, croissant) and oscillatory dynamics or limit cycles (swirling, snaking). If the stationary states have been studied in the past, the numerical challenge of a 3D vesicle's computations delayed the investigations of oscillatory modes. This work also highlights the role of initial conditions in the emergence of nonlinear dynamics, an issue still present whatever the mechanical properties of the membrane.

ACKNOWLEDGMENTS

Centre de Calcul Intensif d'Aix-Marseille is acknowledged for granting access to their high-performance computing resources. A.F., C.M., and M.L. thank CNES (Centre National d'Etudes Spatiales) for financial support that provided access to microgravity data. A.F. and C.M. thank the French-German university program "Living Fluids" (Grant

CFDA-Q1-14). P.G.C., M.J., M.L., and J.L. thank ANR for financial support through Grants No. ANR-18-CE06-0008 and No. ANR-11-LABX-0030, respectively.

-
- [1] P. M. Vlahovska, T. Podgorski, and C. Misbah, Vesicles and red blood cells in flow: From individual dynamics to rheology, *C. R. Phys.* **10**, 775 (2009).
- [2] D. Agarwal and G. Biros, Shape dynamics of a red blood cell in Poiseuille flow, *Phys. Rev. Fluids* **7**, 093602 (2022).
- [3] S. M. Recktenwald, K. Graessel, F. M. Maurer, T. John, S. Gekle, and C. Wagner, Red blood cell shape transitions and dynamics in time-dependent capillary flows, *Biophys. J.* **121**, 23 (2021).
- [4] O. du Roure, A. Lindner, E. N. Nazockdast, and M. J. Shelley, Dynamics of flexible fibers in viscous flows and fluids, *Annu. Rev. Fluid Mech.* **51**, 539 (2019).
- [5] L. Zhu and F. Gallaire, Bifurcation Dynamics of a Particle-Encapsulating Droplet in Shear Flow, *Phys. Rev. Lett.* **119**, 064502 (2017).
- [6] S. K. Veerapaneni, Y.-N. Young, P. M. Vlahovska, and J. Bławzdziwicz, Dynamics of a Compound Vesicle in Shear Flow, *Physical review letters* **106**, 158103 (2011).
- [7] K. P. Sinha and R. M. Thakkar, A theoretical study on the dynamics of a compound vesicle in shear flow, *Soft Matter* **15**, 6994 (2019).
- [8] A. M. Slowicka, E. W. Wajnryb, and M. L. Ekiel-Jezewska, Dynamics of flexible fibers in shear flow, *J. Chem. Phys.* **143**, 124904 (2015).
- [9] J. Dupire, C. Lartigue, and A. Viallat, Full dynamics of a red blood cell in shear flow, *Proc. Natl. Acad. Sci. USA* **109**, 20808 (2012).
- [10] D. Liu, Z. Zhang, R. Wang, and J. Hu, Stability and deformation of vesicles in a cylindrical flow, *Langmuir* **38**, 629 (2022).
- [11] P. Bagchi and R. M. Kalluri, Dynamics of nonspherical capsules in shear flow, *Phys. Rev. E* **80**, 016307 (2009).
- [12] S. K. Doddi and P. Bagchi, Lateral migration of a capsule in a plane Poiseuille flow in a channel, *Int. J. Multiph. Flow* **34**, 966 (2008).
- [13] J. Gubspun, P.-Y. Gires, C. d. Loubens, D. Barthes-Biesel, J. Deschamps, M. Georgelin, M. Leonetti, E. Leclerc, F. Edwards-Lévy, and A.-V. Salsac, Characterization of the mechanical properties of cross-linked serum albumin microcapsules: effect of size and protein concentration, *Colloid and Polym. Sci.* **294**, 1381 (2016).
- [14] E. Häner, M. Heil, and A. Juel, Deformation and sorting of capsules in a T-junction, *J. Fluid Mech.* **885**, A4 (2020).
- [15] T. Lin, Z. Wang, R. Lu, W. Wang, and Y. Sui, A high-throughput method to characterize membrane viscosity of flowing microcapsules, *Phys. Fluids* **33**, 011906 (2021).
- [16] C. Tregouet, T. Salez, C. Monteux, and M. Reyssat, Transient deformation of a droplet near a microfluidic constriction: A quantitative analysis, *Phys. Rev. Fluids* **3**, 053603 (2018).
- [17] C. de Loubens, J. Deschamps, G. Boedec, and M. Leonetti, Stretching of capsules in an elongation flow, A route to constitutive law, *J. Fluid Mech.* **767**, R3 (2015).
- [18] A. Kihm, L. Kaestner, C. Wagner, and S. Quint, Classification of red blood cell shapes in flow using outlier tolerant machine learning, *PLoS Comput. Biol.* **14**, e1006278 (2018).
- [19] A. Guckenberger, A. Kihm, T. John, C. Wagner, and S. Gekle, Numerical-experimental observation of shape bistability of red blood cells flowing in a microchannel, *Soft Matter* **14**, 2032 (2018).
- [20] B. Kaoui, N. Tahiri, T. Biben, H. Ez-Zahraouy, A. Benyoussef, G. Biros, and C. Misbah, Complexity of vesicle microcirculation, *Phys. Rev. E* **84**, 041906 (2011).
- [21] D. Fedosov, M. Peltomäki, and G. Gompper, Deformation and dynamics of red blood cells in flow through cylindrical microchannels, *Soft Matter* **10**, 4258 (2014).
- [22] A. K. Dasanna, J. Mauer, G. Gompper, and D. A. Fedosov, Importance of viscosity contrast for the motion of erythrocytes in microcapillaries, *Front. Phys.* **9**, 666913 (2021).
- [23] W. L. Zeile, F. Zhang, R. B. Dickinson, and D. L. Purich, Listeria's right-handed helical rocket-tail trajectories: mechanistic implications for force generation in actin-based motility, *Cell Motil. Cytoskeleton* **60**, 121 (2005).
- [24] V. B. Shenoy, D. T. Tambe, A. Prasad, and J. A. Theriot, A kinematic description of the trajectories of listeria monocytogenes propelled by actin comet tails, *Proc. Natl. Acad. Sci. USA* **104**, 8229 (2007).
- [25] V. Ronfard and Y. Barrandon, Migration of keratinocytes through tunnels of digested fibrin, *Proc. Natl. Acad. Sci. USA* **98**, 4504 (2001).
- [26] U. Seifert and S. A. Langer, Viscous modes of fluid bilayer membranes, *Europhysics Letters* **23**, 71 (1993).
- [27] T. R. Powers, Dynamics of filaments and membranes in a viscous fluid, *Rev. Mod. Phys.* **82**, 1607 (2010).
- [28] G. Boedec, M. Jaeger, and M. Leonetti, Pearling instability of a cylindrical vesicle, *J. Fluid Mech.* **743**, 262 (2014).
- [29] R. Dimova, U. Seifert, B. Pouligny, S. Förster, and H.-G. Döbereiner, Hyperviscous diblock copolymer vesicles, *Eur. Phys. J. E* **7**, 241 (2002).
- [30] M. Dionzou, A. Morère, C. Roux, B. Lonetti, J.-D. Marty, C. Mingotaud, P. Joseph, D. Goudouneche, B. Payré, M. Léonetti, and A.-F. Mingotaud, Comparison of methods for the fabrication and the characterization of polymer self-assemblies: what are the important parameters?, *Soft Matter* **12**, 2166 (2016).
- [31] C. Pozrikidis, *Boundary integral and singularity methods for linearized viscous flow* (Cambridge University Press, Cambridge, England, 1992).

- [32] T. Biben, A. Farutin, and C. Misbah, Three-dimensional vesicles under shear flow: Numerical study of dynamics and phase diagram, *Phys. Rev. E* **83**, 031921 (2011).
- [33] H. Zhao, A. P. Spann, and E. S. G. Shaqfeh, The dynamics of a vesicle in a wall-bound shear flow, *Phys. Fluids* **23**, 121901 (2011).
- [34] G. Boedec, M. Leonetti, and M. Jaeger, 3D vesicle dynamics simulations with a linearly triangulated surface, *J. Comput. Phys.* **230**, 1020 (2011).
- [35] J. M. Barakat and E. S. G. Shaqfeh, The steady motion of a closely fitting vesicle in a tube, *J. Fluid Mech.* **835**, 721 (2018).
- [36] D. Agarwal and G. Biros, Stable shapes of three-dimensional vesicles in unconfined and confined poiseuille flow, *Phys. Rev. Fluids* **5**, 013603 (2020).
- [37] M.-C. Lai and Y. Seol, A stable and accurate immersed boundary method for simulating vesicle dynamics via spherical harmonics, *J. Comput. Phys.* **449**, 110785 (2022).
- [38] G. Boedec, M. Leonetti, and M. Jaeger, Isogeometric FEM-BEM simulations of drop, capsule and vesicle dynamics in stokes flow, *J. Comput. Phys.* **342**, 117 (2017).
- [39] J. Lyu, P. G. Chen, G. Boedec, M. Leonetti, and M. Jaeger, An isogeometric boundary element method for soft particles flowing in microfluidic channels, *Comput. Fluids* **215**, 104786 (2021).
- [40] G. Boedec, M. Jaeger, and M. Leonetti, Sedimentation-induced tether on a settling vesicle, *Phys. Rev. E* **88**, 010702(R) (2013).
- [41] G. Coupier, A. Farutin, C. Minetti, T. Podgorski, and C. Misbah, Shape Diagram of Vesicles in Poiseuille Flow, *Phys. Rev. Lett.* **108**, 178106 (2012).
- [42] A. Farutin and C. Misbah, Symmetry breaking and cross-streamline migration of three-dimensional vesicles in an axial Poiseuille flow, *Phys. Rev. E* **89**, 042709 (2014).
- [43] B. Kaoui, G. Biros, and C. Misbah, Why do Red Blood Cells Have Asymmetric Shapes Even in a Symmetric Flow? *Phys. Rev. Lett.* **103**, 188101 (2009).
- [44] See Supplemental Material at <http://link.aps.org/supplemental/10.1103/PhysRevFluids.8.L021602> for movies of snaking and swirling.
- [45] V. Vitkova, M. Mader, and T. Podgorski, Deformation of vesicles flowing through capillaries, *Europhysics Letters* **63**, 398 (2004).
- [46] S. H. Strogatz, *Nonlinear Dynamics and Chaos* (CRC Press, Boca Raton, FL, 2018).
- [47] R. Dimova, Recent developments in the field of bending rigidity measurements on membranes, *Adv. Colloid Interface Sci.* **208**, 225 (2014).
- [48] H. Wu, M. Thiébaud, W.-F. Hu, A. Farutin, S. Rafai, M.-C. Lai, P. Peyla, and C. Misbah, Amoeboid motion in confined geometry, *Phys. Rev. E* **92**, 050701(R) (2015).
- [49] H. Wu, A. Farutin, W.-F. Hu, M. Thiébaud, S. Rafai, P. Peyla, M.-C. Lai, and C. Misbah, Amoeboid swimming in a channel, *Soft Matter* **12**, 7470 (2016).